Electronic Supplementary Information

Soap Film Inspired Mechanical Metamaterials Approaching Theoretical Bound of Stiffness across Full Density Range

Biwei Deng[1], Gary J. Cheng[1,2,]*

[1]School of Industrial Engineering, Purdue University, West Lafayette, IN, 47907, USA

[2]Birck Nanotechnology Center, Purdue University, West Lafayette, IN, 47907, USA

[*]Correspondent authors. E-mail: gjcheng@purdue.edu

Construction of the CMC surfaces

The construction of the CMC surfaces (including TPMSs) is conducted via Surface Evolver[1]. Below are the steps of the constructions.

1) One need to input the initial conditions in Surface Evolver, including defining a tetrahedron cell bound by mirror planes of a particular cubic symmetry and creating a starting meshed surface in the tetrahedron. For example, in order to obtain the TPMS-SP or SP-CMC, a tetrahedron cell with vertex of (0,0,0), (0,0,1), (1,0,1) and (1,1,1) is defined; a starting surface of square plane with vertex of (0.5,0.5,0.5); (0.5,0,0.5); (0.5,0,1) and (0.5,0.5,1) is created. Meshing the starting surface can be done by command r in Surface Evolver. Parameters for other symmetries are listed in Table. S1.

2) The meshed target surface is evolved by repeatedly refining the mesh (command r) and performing numerical iterations (command g). The numerical iterations are reducing the area total of the surface while the four edges of the surface are constrained within the planes of the tetrahedron. To give a reference mesh density for a smooth surface, TPMS-SP has 256 triangle elements in the bounding tetrahedron and 12288 elements in a full unit cell.

3) When seeking for CMC surfaces, a volumetric constraint is necessary. For example, in Figure S1, the tetrahedron can be split by the ZMC surface into V_1 and V_2. In this SP case, $V_1 = V_2$. To obtain SP-CMC for the volume fraction of x, we need two CMC surface sandwiching the volume. For the CMC surface on the left (red) side, one can either set the volume on the left (red) side to be $(1-x)V_1$ or the right (blue) side to be (V_2-xV_1), depending on how the surface integral is handled in the software. Note that the volume constraint is not necessary in obtaining TPMSs and should be set before the evolving of surfaces for CMC surfaces.

4) After CMC surfaces are obtained on both the left (red) and right (blue) side, the two surfaces are output to AutoCAD. The same tetrahedron cell is drawn and the volume sandwiched by the two evolved surfaces are carved out as the starting block for SP-CMC.

5) Starting blocks of either TPMS-SP or SP-CMC are mirrored multiple times to obtain a full unit cell.

It is worth noting that the paired CMC surfaces in the IWP and FRD cases do not necessarily share the same mean curvature. This is because the increment of the mean curvature as the CMC surfaces offset is likely not linearly correlated to the amount of the induced volume change. Furthermore, it is also possible to present another evolving strategy that ensures the paired CMC surfaces to have the same mean curvature at a targeted sandwiched volume fraction. However, such strategy and the strategy of linear volume change will output results that are reasonably close, despite that the latter generally requires less numerical efforts. Therefore, we have chosen the linear volume method.

Gyroid surfaces are an exception in our construction of CMC surfaces. The original gyroid surface can be generated in the periodic mode of the software. But the offset CMC surface based on gyroid surface is not achievable using the previously mentioned method. This is because there are no mirror planes in gyroid symmetry. As a result, we only used the original gyroid surfaces in our numerical simulation. For the generation of CMC surfaces originated from an initial gyroid, one should look to another report[2].

Numerical modelling

The numerical simulations of finite element modelling in this work are using the commercial software Abaqus/standard. The shell surface or outer surfaces of the solid structures are generated by Surface Evolver. Then these surfaces are output to AutoCAD to form shells or solids. Eventually the geometries are converted into numerical simulations.

For the simulation of the thin TPMS shells, conventional shell elements are used. Meshes of mixed S4R/S3 (S4R dominating) is generated. For the simulation of the thick CMC structures, meshes of C3D8R or C3D10 is used. Periodic boundary conditions are used in the probing of force response while three type of quasi-static deformations (hydrostatic, uniaxial or shear deformation) are applied in the models. To ensure the periodic boundary conditions are properly set, the mesh of the starting building block (within the tetrahedron) is generated first. The mesh of the full unit cell is obtained by multiple mirroring operations of the meshed building block. This way the nodes on the boundary edges or surfaces in the positive and negative directions are in pairs; and periodic boundary conditions can be assigned to these node pairs. Effective mechanical properties are then calculated based on the force response of each structure under deformations. Mesh densities are tested until the output force is stable. The Poisson's ratio of the materials is set to be 0.24.

Experimental verification

In order to verify the numerical models with experimental measurements, samples are printed by the resin-based stereolithography printer (B9Creator), so that the solid phase in our metamaterials are printed with no porosity. Five categories of structures (SP-CMC, SD-CMC, FRD-CMC, IWP-CMC and ISO-CMC) are printed; each category contained 2 or 3 groups of samples divided by varied designed densities. At least 3 samples for each group are printed and measured for their Young's moduli. The samples are printed in the shape of cubes with the size of 25 mm. Each cube contains 4*4*4=64 unit cells. B9R-2-Black and B9R-3-Emerald resins from B9Creations are used as the base materials. To measure the intrinsic Young's moduli of these two resins, cylindrical compression samples (R=7.5mm, H=22mm) are printed in groups of 3. All the samples are compressed by a MTS810 materials test system at a strain rate of $8*10^{-4}$. The linear part in the stress-strain response is used for the calculation of Young's moduli. The relative densities of the CMC samples are calculated using their weights divided by the measured density from the cylindrical standard samples. Depending on the feature size and capability of the 3D printer,

samples of the same group (with the same input CAD file) could have varied weights, and therefore varied relative densities.

It is worth noting that although the intrinsic Poisson's ratios of the resin materials are unknown (possibly not equal to the default value in our models), the verification of our numerical models is not affected. Because in our numerical models, we find that the change of Poisson's ratio alone (without changing the Young's moduli) does not affect the effective Young's moduli of our structures.

Analytical determination of the bulk moduli of TPMSs

For the HS upper bound for bulk moduli of a two-phase material comprised of solid and void, considering only the linear term in Taylor series, we know that

$$K_{HS+} = \frac{4K_2G_2}{3K_2 + 4G_2}x_2 = \frac{2E_2}{9(1-\nu_2)}x_2 \tag{S1}$$

Here K_2, G_2, E_2, ν_2 and $x_2$stands for the bulk modulus, shear modulus, Young's modulus, Poisson's ratio and volume fraction of the solid isotropic phase.

Suppose we have a thin shell structure under hydrostatic tension. that is under 'ideal stretching', which means a universal biaxial strain ε_{eff} is imposed along orthogonal directions. It is convenient seen that the average elastic energy stored in such 'ideal stretching' shell is

$$\overline{U} = \frac{E_2\varepsilon_{eff}^2}{1-\nu_2} \tag{S2}$$

Here the energy is averaged by the solid phase volume x_2V. On the other hand, the elastic energy averaged by the total volume is $x_2\overline{U}$. Since imposed strain is hydrostatic tension the relation between the effective modulus K_{eff} and $x_2\overline{U}$ is

$$x_2\overline{U} = \frac{9}{2}K_{eff}\varepsilon_{eff}^2 \tag{S3}$$

Compare these two expressions, we have

$$K_{eff} = \frac{2E_2}{9(1-\nu_2)}x_2 \tag{S4}$$

Apparently, 'ideal stretching' state is only valid when the shell is thin, which means $x_2 \to 0$. Still we will have

$$K_{eff} = K_{HS+} \tag{S5}$$

Additional mechanical properties

We have concluded these mechanical properties for 5 types of TPMSs and each TPMS is compared to 5 HLs with varied aspect ratios. The surface areas within one unit cell of unit length is summarized in Table S2. These values are further used to calculate the relative densities of the examined structures of a given thickness.

Because the structures in this paper are limited to cubic symmetry, their elastic tensors can be reduced to 3 independent variables. Our numerical models probe the Young's modulus E, bulk modulus K and shear modulus G of each structure. Further the Zener ratios and Young's moduli along different orientations[3] can be calculated by

$$Z = \frac{G(9K - E)}{3KE} \tag{S6}$$

and

$$\frac{1}{E'} = \frac{1}{E} + \frac{9KG - EG - 3KE}{6KEG}((cos\theta cos\varphi)^4 + (sin\theta cos\varphi)^4 + sin\varphi^4 - 1) \tag{S7}$$

The angle θ and φ of the rotation transformation are shown in Figure S2.

These mechanical properties are concluded in Figure S3&S4.

Like the TPMS cases, we have obtained the Young's moduli along different orientations for CMC structures as well, as shown in Figure S6.

Connections to theoretical works

As mentioned in the main text, the problem of optimal bounds for conductivity or elasticity of multi-phase composite has been extensively explored by mathematicians. Although the actual bounds and their attainability have been largely discussed, especially for two-phase materials, an attaining microstructure, which is single scale, periodic and practically realizable, is rarely reported. However, among the theoretical studies, it is worth noting that the theory of E-closure addresses the optimal microstructure generation with a certain degree of flexibility. The studies associated to the E-closure problems provided analytical solutions for 2D cases and numerical solutions for 3D cases. For example, one of these 3D solutions provided a similar microstructure[4] to the cubic foam structure except with smooth edges. We observe in these results that such numerically approximated structures are all closed cell microstructures, meaning that there is always phases of finite volumes completely wrapped by other phases. To the best of the authors' knowledge, no open-cell microstructure, which consists of only two phases of infinite volumes, has been proposed via theoretical tools. Therefore, since it is not yet achievable to have an analytical solution for the problem of 3D optimal composite microstructure, our results reported here can serve well as a new starting mesh for further numerical optimization under theoretical tools, such as E-closure methods.

References

1. Brakke, K. A. The surface evolver. *Exp. Math.* 1992, **1**, 141-165.
2. Große-Brauckmann, K. Gyroids of Constant Mean Curvature. *Exp. Math.* 1997, **6**, 33–50.
3. Wortman, J. J. & Evans, R. A. Young's modulus, shear modulus, and poisson's ratio in silicon and germanium. *J. Appl. Phys.* 1965, **36**, 153–156.
4. Liu, L., James, R. D. & Leo, P. H. Periodic inclusion - Matrix microstructures with constant field inclusions. *Metall. Mater. Trans. A.* 2007, **38**, 781-787.

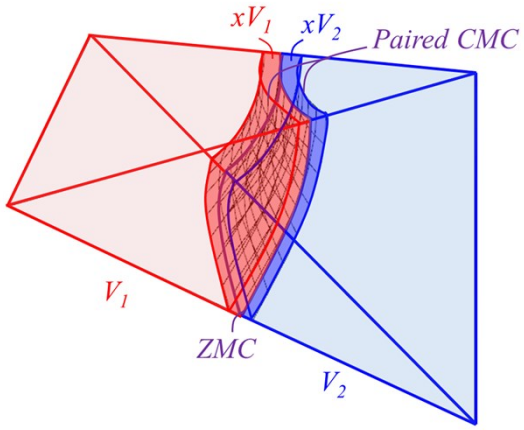

Figure S1. Schematic figure of how volume is added while forming CMC structures. Here in the SP case, V_1=V_2.

Table S1. Tetrahedron and starting surface coordinates for generation of CMC surfaces.

	Tetrahedron vertex	Starting surface vertex
SP	(0,0,0); (0,0,1); (1,0,1); (1,1,1)	(0.5,0.5,0.5); (0.5,0,0.5); (0.5,0,1); (0.5,0.5,1)
IWP	(0,0,0); (0,0,1); (1,0,1); (1,1,1)	(0,0,0.5); (0.5,0,0.5); (1,0.5,1); (0.5,0.5,1)
FRD	(0,0,0); (0,0,1); (1,-1,1); (1,1,1)	(1,0,1); (0.5,-0.5,0.5); (0,0,0.5); (0.5,0.5,1)
SD	(0,0,0); (0,0,2); (1,-1,1); (1,1,1)	(1,0,1); (0.5,0.5,0.5); (0,0,1); (0.5,-0.5,1.5)

Table S2. Surface areas of examined TPMSs and HLs in a cubic unit cell of unit length.

	TPMS	HL1	HL2	HL3	HL4	HL5
GY	1.550	0.805	1.100	1.365	1.516	1.552
SP	1.173	0.987	1.131	1.197	1.174	1.084
SD	1.921	1.274	1.544	1.742	1.878	1.925
IWP	1.735	1.099	1.595	1.841	1.742	1.420
FRD	2.421	1.877	2.354	2.644	2.660	2.413

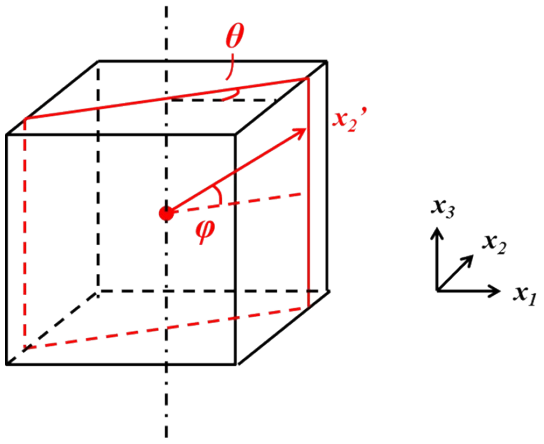

Figure S2. Rotational transformation ($^{x_2 \rightarrow x_2'}$) used for plotting polar graphs of Young's moduli.

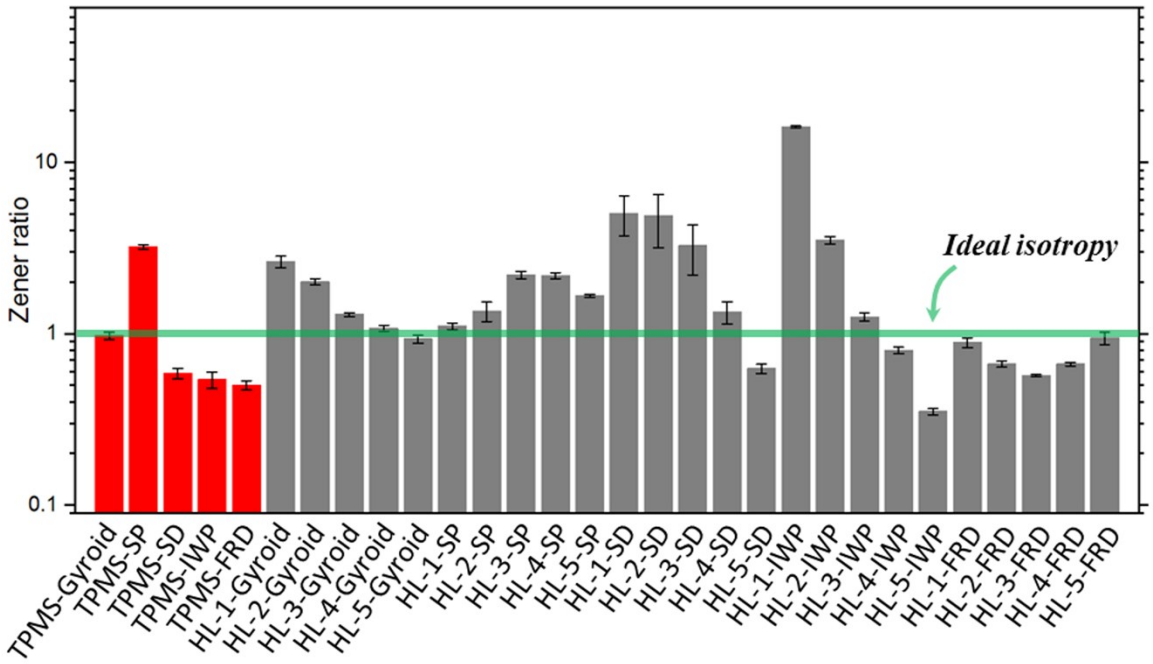

Figure S3. Zener ratios of examined TPMS and HL shell structures.

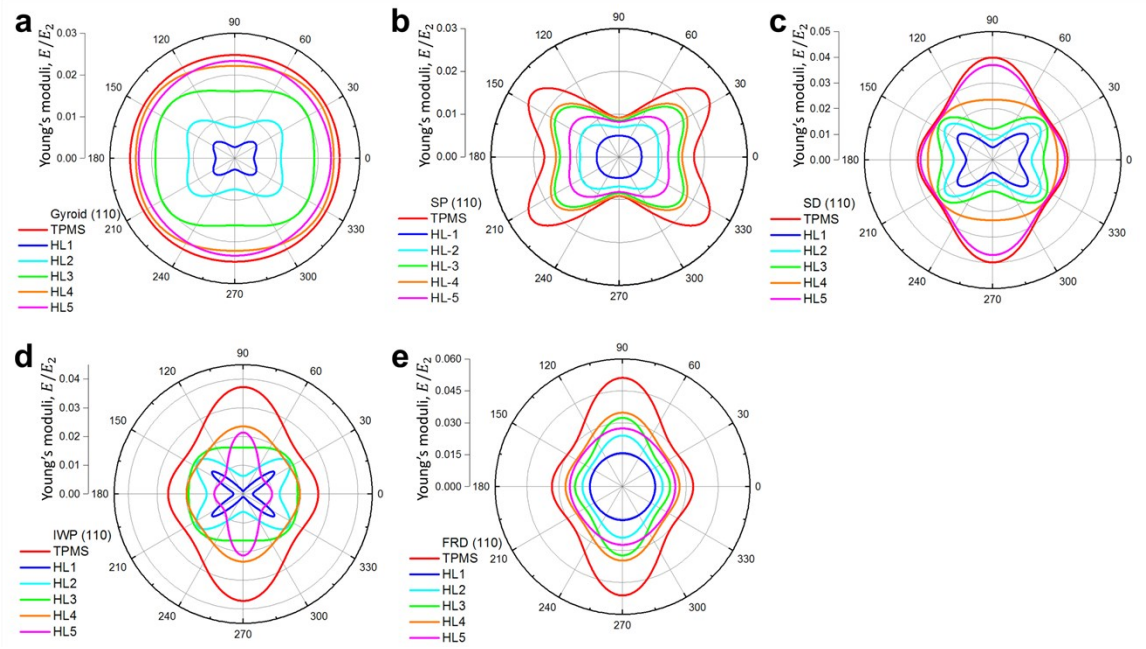

Figure S4. Polar graphs showing the Young's moduli along varied orientations (0°=[110]; 90°=[100]; 35.26°=[111]) of the TPMSs compared to the reference HLs of the same thickness (0.05). a) Gyroid shell structure vs its reference HLs; b) SP shell structure vs its reference HLs; c) SD shell structure vs its reference HLs; d) IWP shell structure vs its reference HLs; e) FRD shell structure vs its reference HLs.

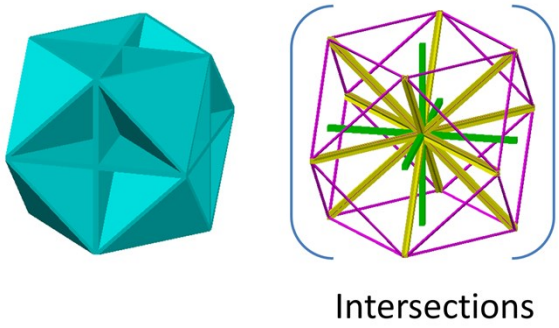

Figure S5. Cubic-octet foam structure and its self-intersected volumes.

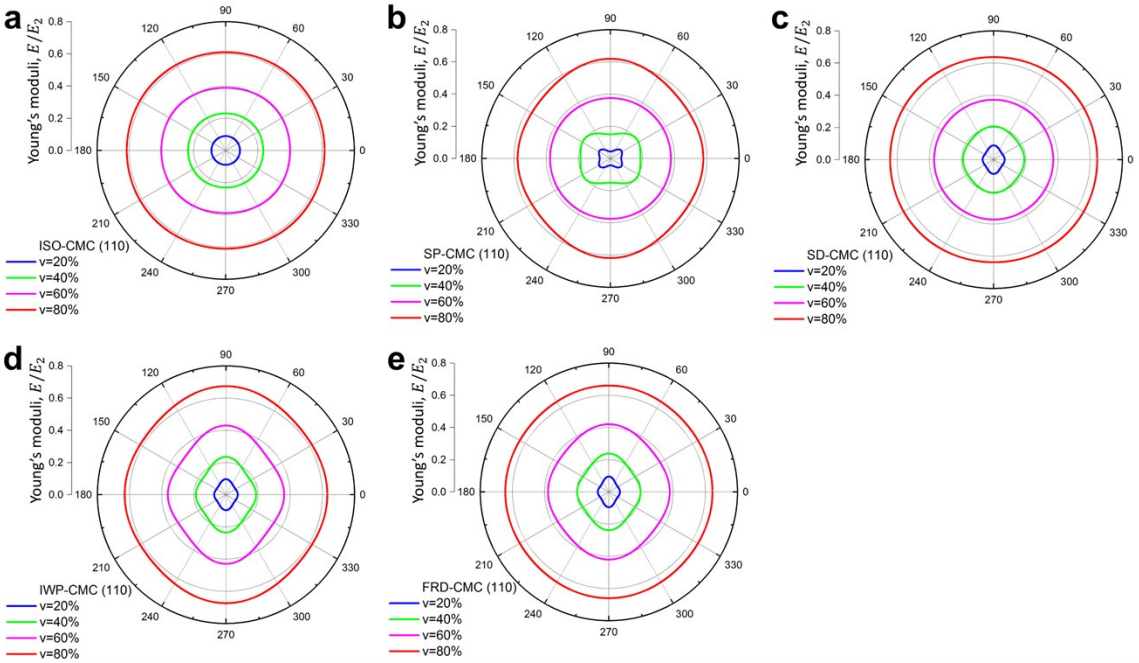

Figure S6. Polar graphs showing the Young's moduli along varied orientations (0°=[110]; 90°=[100]; 35.26°=[111]) of the CMC structure at various relative densities. a) ISO-CMC; b) SP-CMC; c) SD-CMC; d) IW-CMC; e) FRD-CMC.

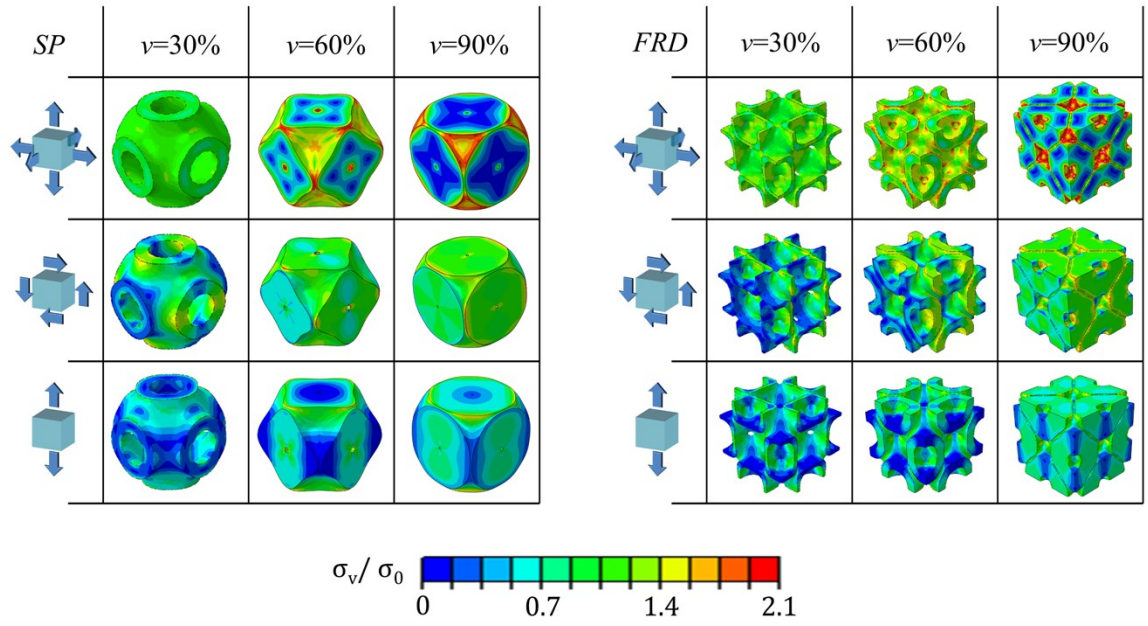

Figure S7. Von Mises stress distributions in the CMC structures under different imposed deformations. Here, $\sigma_0 = \frac{E\varepsilon_{ij}}{1-\nu}$ and $\varepsilon_{ij} = 5\times10^{-4}$.